Calcium isotopes as a record of the marine calcium cycle versus carbonate diagenesis during the late Ediacaran

Calcium isotopes as a record of the marine calcium cycle versus carbonate diagenesis during the late Ediacaran

Rosalie Tostevin[1*], Harold J. Bradbury[2], Graham A. Shields[3], Rachel A. Wood[4], Fred Bowyer[4], Amelia M. Penny[4,5], Alexandra V. Turchyn[2]

[1]Department of Geological Sciences, University of Cape Town, University Avenue South, Cape Town, South Africa, 7701

[2]Department of Earth Sciences, University of Cambridge, Downing Street, Cambridge, CB2 3EQ, UK

[3]Department of Earth Sciences, University College London, Gower Street, London, WC1E 6BT, UK

[4]School of Geosciences, University of Edinburgh, James Hutton Road, Edinburgh, EH9 3FE, UK

[5]Finnish Museum of Natural History, University of Helsinki, P. O. Box 44 (Jyrängöntie 2), 00014 Helsinki, Finland

*Rosalie.tostevin@uct.ac.za

Highlights

- $\delta^{44}Ca$ from limestones aged ~550–539 Ma that host the earliest skeletal animal fossils
- Negative shift in $\delta^{44}Ca$ that lasted at least 11–14 Myrs
- Unlikely to record a transition towards more sediment-buffered carbonate diagenesis

- May record enhanced continental weathering or evaporite deposition
- May record a change in timing of dolomitisation

Keywords: Calcium isotopes; carbonate rocks; marine calcium cycle; analytical methods; Ediacaran; biomineralisation

Abstract

Calcium isotope ratios in ancient carbonate rocks can provide insight into the global marine calcium cycle as well as local conditions during carbonate mineral precipitation and diagenesis. We compare two extraction techniques for the separation of calcium from other ions before $\delta^{44}Ca$ analysis, using an automated ion chromatograph and using manual gravity columns. The two techniques produce the same $\delta^{44}Ca$ within error (2σ). We present 31 $\delta^{44}Ca$ analyses of carbonate rocks from the Nama Group, Namibia, which record a negative shift in $\delta^{44}Ca$ of 0.35‰ between ~550 and ~547 Ma, from −1.25‰ to −1.60‰, followed by persistently low $\delta^{44}Ca$ (−1.48 ± 0.06‰) between ~547 and 539 Ma. Very low $\delta^{44}Ca$ (<−1.5‰) are commonly interpreted to represent the preservation of local aragonite that has recrystallized to calcite under sediment-buffered conditions (where the composition of the diagenetic carbonate product is determined mainly by the original sediments). The shift in $\delta^{44}Ca$ across the Nama Group could therefore represent a change from fluid-buffered diagenesis (where the composition of the diagenetic carbonate mineral is determined mainly by the fluid) to sediment-buffered diagenesis. However, this interpretation is not consistent with either potential geochemical indicators of diagenesis (e.g., $\delta^{18}O$), or changes in large-scale fluid-flow as predicted from sequence stratigraphy.

We consider alternative interpretations for generating changes in the $\delta^{44}Ca$ of ancient carbonate rocks including enhanced continental weathering, increases in evaporite deposition, and changes in the style of dolomitisation.

1. Introduction

Calcium isotope ratios (the ratio of $^{44}Ca/^{40}Ca$ and reported versus a standard as $\delta^{44}Ca$) measured in ancient carbonate minerals and rocks such as limestone and dolomite, offer a potential tool to investigate the workings of the ancient marine calcium cycle as well as to explore carbonate mineral deposition and subsequent diagenesis (Blättler et al., 2012, 2011; Bradbury and Turchyn, 2018; Higgins et al., 2018; Husson et al., 2015). The calcium isotope ratio of seawater, $\delta^{44}Ca_{SW}$, is controlled by the balance of fluxes of calcium into and out of seawater, and the calcium isotopic composition of those fluxes. The main source of calcium to seawater is riverine input, although hydrothermal fluids may account for ~17% of total calcium input to the ocean (Tipper et al., 2010). The main output flux is the deposition of carbonate-bearing sediments, but evaporite deposition and alteration of oceanic crust are also important sinks for calcium.

Calcium isotopes preserved in carbonate rocks reflect both the $\delta^{44}Ca$ of the seawater or fluid from which carbonate minerals precipitated, as well as the kinetic calcium isotope fractionation during precipitation ($\Delta^{44}Ca_{local}$), which is determined by the carbonate mineral precipitating (e.g., calcite, aragonite or dolomite) and its rate of precipitation (Blättler et al., 2012; Tang et al., 2008). At steady state, the dominant control on the calcium isotope composition of seawater ($\delta^{44}Ca_{SW}$) is the average $\delta^{44}Ca$ of global buried carbonate minerals ($\delta^{44}Ca_{global}$). However, carbonate rocks are also the major archive used

to reconstruct seawater $\delta^{44}Ca$ in deep time. Therefore, to interpret $\delta^{44}Ca_{SW}$ from $\delta^{44}Ca$ in carbonate rocks, a *local* calcium isotope fractionation factor must be assumed based on the inferred original (primary) and dominant mineralogy. Although early $\delta^{44}Ca$ data were commonly interpreted to reflect changes in the global calcium cycle, i.e., the relative sources and sinks of calcium to the ocean (Blättler et al., 2012, 2011; Hinojosa et al., 2012; Payne et al., 2010), more recently, $\delta^{44}Ca$ data have been interpreted to record calcium isotope signatures acquired during diagenesis at the site of sediment lithification (Ahm et al., 2019, 2018; Higgins et al., 2018; Husson et al., 2015).

The late Ediacaran was a time of dramatic environmental and ecological change, including oscillating redox conditions, extensive evaporite deposition, and the appearance of skeletal animals (Fike and Grotzinger, 2008; Tostevin et al., 2019; Wood, 2011; Wood et al., 2017b). We present $\delta^{44}Ca$ data from the Nama Group, Namibia, that record a negative shift in $\delta^{44}Ca$ of ~0.35‰ between ~550 and ~547 Ma, followed by persistently low $\delta^{44}Ca$ (−1.48 ± 0.06‰) from ~547 to ~539 Ma. We combine these data with other major element and isotopic geochemical data from the same samples to evaluate several potential explanations for this $\delta^{44}Ca$ shift, and discuss the application of calcium isotope systematics in deep time.

2. Geological and geochemical context

2.1 Sequence stratigraphy and diagenetic history of the Nama Group

The Nama Group was deposited in two inter-connected sub-basins, the southern Witputs and the northern Zaris, separated by a zone of depositional thinning representing the "Osis Arch" paleo-bathymetric high (Germs, 1974). Unrestricted connection to the open ocean has been suggested because of the preservation of $\delta^{13}C$ excursions in time-equivalent sections, and normal marine rare earth element signatures (Bowyer et al., 2017; Kaufman et al., 1991; Tostevin et al., 2016b; Wood et al., 2015). The Zaris Formation (Kuibis Subgroup) in the Zaris sub-basin was sampled at Zebra River Farm, and the Urusis Formation (Schwarzrand Subgroup) in the Witputs sub-basin was sampled at Swartkloofberg Farm and at Swartpunt Farm. The base of the Nama Group is diachronous, but has been estimated to have been deposited between 553 and 550 Ma (Ries et al., 2009; Saylor et al., 1998). An ash bed in the Hoogland Member yields a depositional age of 547.32 ± 0.65 Ma (Bowring et al., 2007; Grotzinger et al., 1995). Therefore, deposition of the Omkyk and Hoogland members of the Zaris Formation likely spans 3–6 Myrs. Ash beds at Swartpunt Farm yield ages of 540.095 ± 0.099 Ma and 538.99 ± 0.21 Ma for the top of the Schwarzrand Subgroup (Linnemann et al., 2019). Overall, the Nama Group therefore spans 11–14 Myrs.

The Nama Group hosts terminal Ediacaran skeletal fauna, *Cloudina*, *Namacalathus* and *Namapoikia*, as well as soft-bodied Ediacaran fossils and increasing trace fossil evidence for motility towards the top of the section (Germs, 1972; Grant, 1990; Grotzinger et al., 2000; Jensen et al., 2000; Wood et al., 2002). At the deep inner-ramp locality, Zebra River, the Lower Omkyk Member is dominated by grainstones. In the transgressive systems

tract of the Upper Omkyk Member, thrombolite-stromatolite reefs nucleate, forming laterally continuous biostrome layers (Grotzinger et al., 2000). *Cloudina* and *Namacalathus* can be found within thrombolite heads and lag beds within inter-reef shales. Towards the top of the Upper Omkyk Member the section shallows into grainstone-dominated facies with subordinate shale horizons, containing thinner, discontinuous biostrome microbial reef systems, and some large *Namacalathus* <35 mm (Penny et al., 2016). The Hoogland Member contains storm dominated laminites and heterolithics, shallowing towards grainstone-dominated facies.

The Pinnacle Reefs at Swartkloofberg Farm were deposited in a mid-ramp setting within a transgressive systems tract, initiated on the flooded surface of the Huns Platform. After termination of reef growth, the reefs were enveloped by shales, and together these facies form the Feldschuhhorn Member. The Pinnacle Reefs host communities of skeletal animals of varied sizes, including aggregations of *Namacalathus* up to 12 mm in diameter (Wood et al., 2015).

Swartpunt Farm, which encompasses the Spitzkopf Member of the Schwarzrand Subgroup, transitions from low-energy outer-ramp setting at the base, towards an inner-ramp environment, followed by a deepening to outer ramp conditions, and a transition towards a mid- to inner-ramp setting at the top of the section. Thin-bedded calcisiltite beds at the base of Swartpunt host *Namacalathus*, large *Cloudina*, and a diversity of carbonate microbialites, and are interpreted to have been deposited in a low-energy deeper ramp setting (Narbonne et al., 1997; Saylor, 2003). The limestone is overlain by thick beds of green mudstone and coarse sandstone, deposited in a deltaic environment, containing burrows and soft-bodied fossils including *Swartpuntia* and *Pteridinium* (Narbonne et al.,

1997). Overlying this there is a 5–10 m interval of thinly bedded siltstone, sandstone and limestone with ripple cross-lamination, deposited above fair weather wave base in an inner-ramp setting. Overlying shales may represent deepening to an outer-ramp environment. These give way to limestones and dolomites with dm-scale thrombolites, deposited at or below storm wave base in a mid-ramp setting (Jensen and Runnegar, 2005). Towards the top of Swartpunt is a highstand system tract containing flaggy, laminated limestones with small (<5 mm) *Cloudina riemkeae* and thrombolites.

The paragenetic sequence of carbonate rocks from the Nama Group has been described in detail from the *Cloudina* reefs at Driedoornvlagte Farm, coeval in part with the Zebra River section, identifying six successive cement generations (Wood et al., 2018). *Cloudina* are commonly preserved as neomorphosed calcite, with micro-dolomite inclusions, and in some cases are completely dolomitised. Large, acicular cements form botryoids and occlude pore space. These commonly nucleate on skeletal fossils, or intergrow with geopetal sediment, and are interpreted to represent an early marine precipitate of originally aragonitic mineralogy (Grant, 1990). This is followed by a thin, isopachous dolomite cement. This is post-dated by a cloudy, inclusion-rich low-Mg calcite cement, interpreted to have precipitated in pore fluids that were in open contact with seawater. Remaining pore space is occluded by a clear, length-slow, blocky low-Mg, calcite, typical of low-Mg pore waters, suggesting a burial origin. Early marine cements are commonly interpreted to be aragonitic, and later neomorphosed to calcite (Grant, 1990; Grotzinger and James, 2000; Wood et al., 2018).

2.2 Geochemical background of the Nama Group samples

156 The Nama Group was deposited coincident with the final recovery from the Shuram-
157 Wonoka anomaly, an enigmatic global $\delta^{13}C$ excursion famed for reaching unusually low
158 values (around −12‰). The Shuram-Wonoka anomaly has been variably interpreted to
159 result from either: 1) the oxidation of a large pool or reduced carbon such as methane
160 hydrates or dissolved organic carbon (Bjerrum and Canfield, 2011; Husson et al., 2015;
161 Rothman et al., 2003), 2) a global increase in the burial of authigenic carbonate (Cui et al.,
162 2017; Schrag et al., 2013), or 3) globally synchronous changes in burial or meteoric
163 diagenesis (Derry, 2010; Knauth and Kennedy, 2009). Some sections in the Nama Group
164 capture the tail end of the Shuram excursion (e.g., at Brak and Grens; Wood et al., 2015),
165 but the Nama Group at Zebra River captures the post-excursion return to positive $\delta^{13}C$. In
166 the Schwarzrand Subgroup, $\delta^{13}C$ remains stable around 1‰.
167 Iron speciation and cerium anomaly measurements have previously been used in
168 this section as proxies for local water column redox conditions (Tostevin et al., 2016b;
169 Wood et al., 2015). These data indicate that Zebra River was predominantly well-
170 oxygenated, with temporary anoxic-ferruginous periods (Wood et al., 2015), which may
171 reflect the development of sluggish circulation or upwelling of anoxic deeper waters
172 associated with marine transgression (Bowyer et al., 2017). Additionally, positive cerium
173 anomalies suggest that some depositional intervals were oxygen-poor and manganous
174 (Tostevin et al., 2016). The Pinnacle Reefs experienced persistent well-oxygenated
175 conditions (Tostevin et al., 2016b; Wood et al., 2015). Swartpunt was largely oxygenated,
176 with anoxic ferruginous conditions restricted to two highstand carbonate horizons.
177 Sediments containing independent evidence for deposition under an oxygenated water

178 column were selected for this study, and all samples have low total organic carbon (TOC) of
179 <0.2 wt.% (Wood et al., 2015).
180 $\delta^{238}U$ data from carbonate rocks at Zebra River transition from modern-like
181 seawater values (−0.4‰) in the Lower Omkyk Member, to very negative values in the
182 Upper Omkyk and Hoogland Members (−0.81‰) (Tostevin et al., 2019). This has been
183 interpreted and modelled to represent a transition towards globally widespread anoxic
184 bottom waters that covered at least a third of the global sea floor. Further, this $\delta^{238}U$
185 transition appears to be recorded globally in sediments of the same age (Zhang et al.,
186 2018), supporting preservation of a primary global seawater $\delta^{238}U$ signal. Existing sulfur
187 isotope data from carbonate associated sulfate at Zebra River show a general increasing
188 trend in $\delta^{34}S_{CAS}$ from the Omkyk to the Hoogland Members (Tostevin et al., 2017). This
189 correlates with contemporaneous sections from other basins, suggesting a global change in
190 the sulfur cycle that drove an increase in global marine $\delta^{34}S$ (Cui et al., 2016b, 2016a; Fike
191 and Grotzinger, 2008). This has been interpreted to reflect a change in weathering fluxes or
192 sources, and/or an increase in the global pyrite burial flux.

3. Methods

Hand samples were collected at one to five meter intervals along with stratigraphic logs noting lithology and paleoecology. Weathered edges were removed and samples were sawed in half to reveal a fresh surface. Powders from Zebra River for $\delta^{44}Ca$ analysis were drilled with a dremel microdrill, avoiding visually recrystallised areas. Bulk-rock powders were analysed from the Pinnacle Reefs and Swartpunt sections.

Major element concentrations (Sr, Ca, Mg and Mn) in the carbonate portion of the sample were determined using sequential leaching in 2% HNO_3, and analysed via Inductively coupled plasma optical emission spectrometer (ICP-OES) at the Cross-Faculty Elemental Analysis Facility, University College London. The sequential leaching method involves pre-leaching 20% of the sample, followed by a 40% leach that is retained for analysis (method is described in full in Tostevin et al., 2016a). These major element data are available for Zebra River section as well as four other localities in the Nama Group (the Kuibis Subgroup at Brak, Omkyk and Zwartmodder, and the Schwarzrand Subgroup at Swartpunt; Wood et al., 2015). Carbon isotopes have been previously reported in Wood et al., (2015).

These data were used to inform sample selection for calcium isotope analysis. Samples with a wide range of Sr contents, including those that were anomalous compared with adjacent samples, were selected. Selected samples included a range of facies and textures, including microbialites, grainstones and laminites. Dolomitised or impure samples (low $\%CaCO_3$) were avoided. Calcium isotope ($^{44}Ca/^{40}Ca$) analysis was conducted at the University of Cambridge using a Thermo Scientific Triton Plus MC-Thermal Ionisation Mass Spectrometer. Sample aliquots containing six μg of calcium were combined

with a ^{42}Ca-^{48}Ca double–spike at a ratio of 10:1 (sample-to-spike) in acid-cleaned Teflon vials. The 48:42 ratio of the double–spike is 1:1, similar to the optimum ratio of 3:2 for a ^{42}Ca-^{48}Ca double–spike (Rudge et al., 2009). Solid samples were dissolved in dilute ultra-pure acetic acid for 1 h, before being converted to nitrates and then combined with the double spike. The samples were then dried and re-dissolved in 0.5% nitric acid and calcium was separated using either a Dionex ICS 5000$^+$ HPIC coupled with a Dionex AS-AP fraction collector or a gravity column (Bio-Rad AG50W-X8) setup for method validation.

After the separation of the calcium using either the Dionex ICS 5000$^+$ HPIC or the gravity columns, 4 μg of calcium was loaded on an outgassed 0.7 mm Rhenium filament with 0.5 μl of 10% trace metal purity Phosphoric acid as an activator. The samples are run using the analytical method previously described in Bradbury and Turchyn (2018). The average external 2σ standard deviation over nine months on the standard NIST915B was 0.10‰ (n = 82). All $\delta^{44}Ca$ discussed in the text are reported as ratios of ^{44}Ca to ^{40}Ca relative to modern seawater, but in Table 1 the data are also reported relative to other commonly used calcium standards (BSE and 915a).

3.1 Method Validation

Each sample was run for its calcium isotopic composition four times, using two extraction techniques; separating the calcium using an automated ion chromatograph and separating the calcium using manual gravity columns. The samples run using the Thermo Scientific Dionex ICS 5000$^+$ HPIC were run through a high-capacity carboxylate-functionalised column (Dionex CS-16) using 30 mM methyl-sulfonic acid (MSA) at a flow

rate of 1 ml/min. The conductivity of the samples was continuously measured during the separation, and a minimum peak slope of 0.003 μS/s determined the sample collection during a set time window. The method is similar to the published work of Schmitt et al., (2009), and has been published in Bradbury et al., (2018) and Bradbury and Turchyn, (2018).

These analyses were compared to samples that were separated through a traditional gravity column setup using Bio-Rad AG50W-X8 resin. The gravity columns were created from cut down 5 ml pipettes with a reservoir size of 2 ml and with a 20 μm PE frit installed. They were filled to just below 1 ml with slurried AG50W-X8 resin. The columns were pre-cleaned using 2 ml of 4 M HCl, 6 M HNO_3, 4 M HCl and water, before being preconditioned with 1.5 M HNO_3. The columns had a flow rate of approximately 1 ml/hour. The sample was loaded and then eluted with 1.5 M HNO_3. The columns were calibrated by measuring the concentration of the ions eluting off the column using the Dionex ICS 5000^+. The calibration was setup to collect 100% of the calcium and maximise the separation of calcium from magnesium and strontium, whilst at the same time minimising the time taken to complete the column chemistry. Initially a series of twelve carbonate powders from the Nama Group were dissolved in 5% ultrapure acetic acid. An aliquot containing 12 μg of calcium was then spiked at a ratio of 10:1 (sample to spike) with the double spike and dried. The dried sample was re-dissolved in 1.5 M HNO_3 and separated using the calibrated gravity columns. The 4 μg of the collected calcium was loaded per filament either singularly (n=6), in duplicate (n=6), or triplicate (n=12). The measured sample data is shown graphically in Figure 1, where the $\delta^{44}Ca$ from the Dionex ICS 5000^+ HPIC and the column separations are compared.

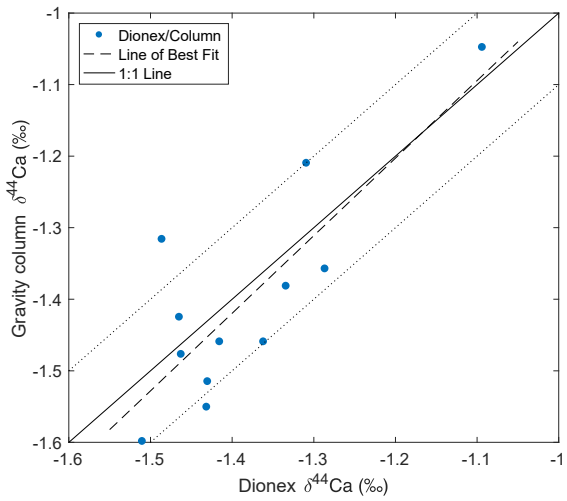

Figure 1: Cross plots of the twelve samples run on the Dionex ICS 5000⁺ and gravity columns (n=12, R^2=0.65, p-value = 0.0119). The dotted lines represent the long-term 2σ of the measurement of calcium isotopes. A t-test comparison of the slopes of the measured data and the 1:1 line shows no statistically significant difference.

4. Results

We report 31 new $\delta^{44}Ca$ analyses from the Nama Group, which range from −1.60‰ to −1.07‰. At Zebra River, $\delta^{44}Ca$ progressively decreases from the base of the section through the Kuibis Subgroup from −1.25‰ to −1.60‰, an overall decrease of 0.35‰ (Figure 2). There is one outlying data point, with a particularly high $\delta^{44}Ca$ of −1.09‰ (at 106 m). At the Pinnacle Reefs and Swartpunt, $\delta^{44}Ca$ remains low through the Schwarzrand Subgroup, between −1.39‰ and – 1.59‰ (average = −1.48 ± 0.06). Two partially

dolomitised samples have a $\delta^{44}Ca$ that is ~0.4‰ higher than the surrounding samples (−1.08‰ at 5 m and −1.07‰ at 10 m), and these have been excluded from consideration due to the known positive $\delta^{44}Ca$ offset associated with dolomitisation (Fantle and DePaolo, 2007; Turchyn and DePaolo, 2011). The samples are all laminite heterolithics, grainstones, microbialites, or recrystallized limestones, and changes in $\delta^{44}Ca$ do not appear to correlate with changes in these lithologies (Figure 2).

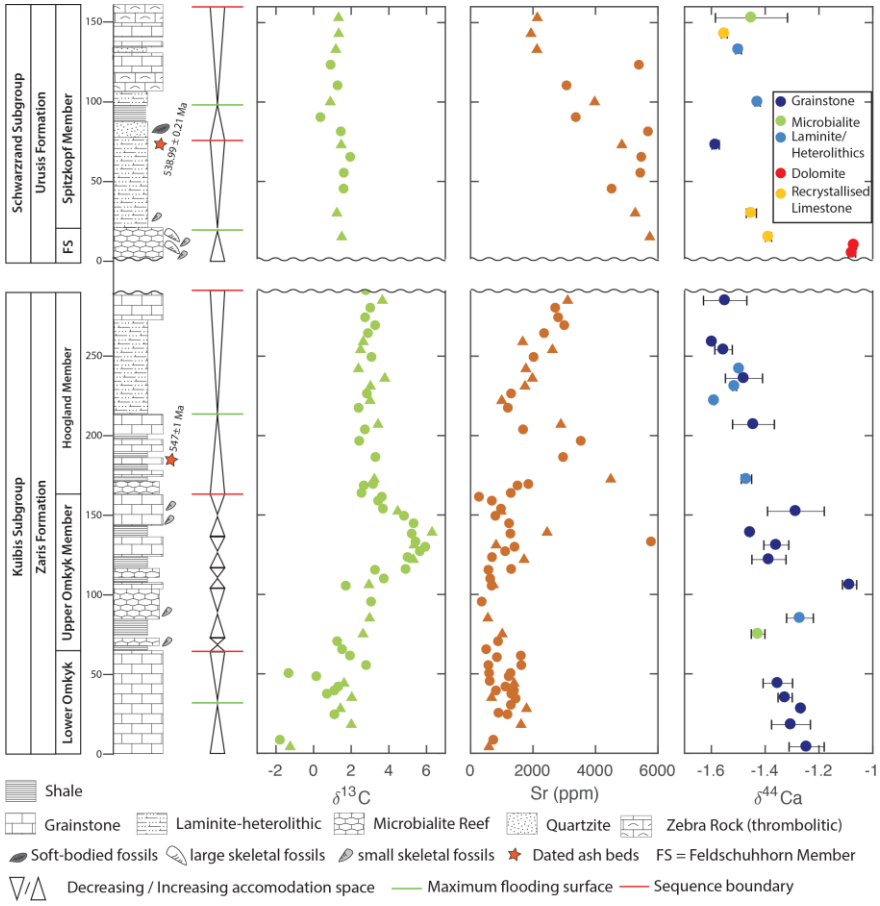

Figure 2: From left to right: Stratigraphic log, sequence stratigraphy, $\delta^{13}C$ data, Sr content and $\delta^{44}Ca$ for the Nama Group. Triangle symbols for $\delta^{13}C$ data and Sr content highlight samples for which there is also $\delta^{44}Ca$ data. The $\delta^{44}Ca$ data are colour coded according to the facies of individual samples. The Kuibis Subgroup was sampled at Zebra River, the Feldschuhhorn Member (FS) was samples at the Pinnacle Reefs, and the Spitzkopf Formation was sampled at Swartpunt Farm. Ash bed dates from Hoogland Member and Spitzkopf Member are from Bowring et al., (2007) and Linnemann et al., (2019). Sequence stratigraphy is from Adams et al., (2005), Saylor (2003) and Saylor et al., (1998). The wavy line in the stratigraphic column does not indicate a substantial erosional unconformity, but an absence of samples from the intervening stratigraphy.

Strontium content in the carbonate rocks is consistent throughout the Omkyk Member, with an average of 1000 ppm, but rises through the Hoogland Member reaching a peak of ~4000 ppm. In the Schwarzrand Subgroup, the strontium content declines from a high of ~6000 ppm to ~2000 ppm close to the Ediacaran-Cambrian boundary. This increase in strontium content is consistent across multiple sections of the Nama Group (Wood et al., 2015; Figure 3). At Zebra River, scatter overprints the overall trend in Sr content, with some exceptionally high values in the middle of the section. $\delta^{44}Ca$ correlates with Sr content (R^2=0.27), $\delta^{34}S_{CAS}$ (R^2=0.53) and $\delta^{18}O$ (R^2=0.40) measured on the same samples at the $P<0.05$ level, but with significant scatter around the trend (Figure 4b, 4f and 4k). In contrast, there is no significant correlation between $\delta^{44}Ca$ and other geochemical data ($P>0.05$), including Mn content, $\delta^{13}C$, TOC and Mg/Ca (Figure 4a and 4c-e).

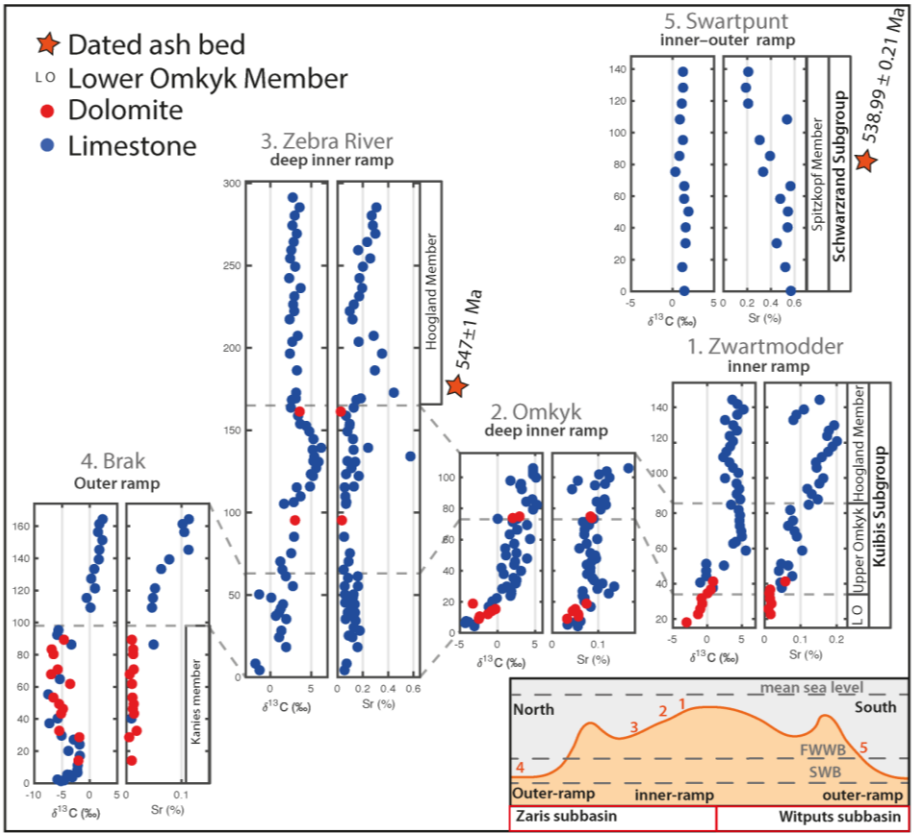

306

307 **Figure 3**: Sr concentrations for four sections from the Kuibis Subgroup, and one section

308 from the Schwarzrand Subgroup. Carbon isotopes from Wood et al., (2015). Ash bed dates

309 from Hoogland Member and Spitzkopf Member are from Bowring et al., (2007) and

310 Linnemann et al., (2019).

311

312

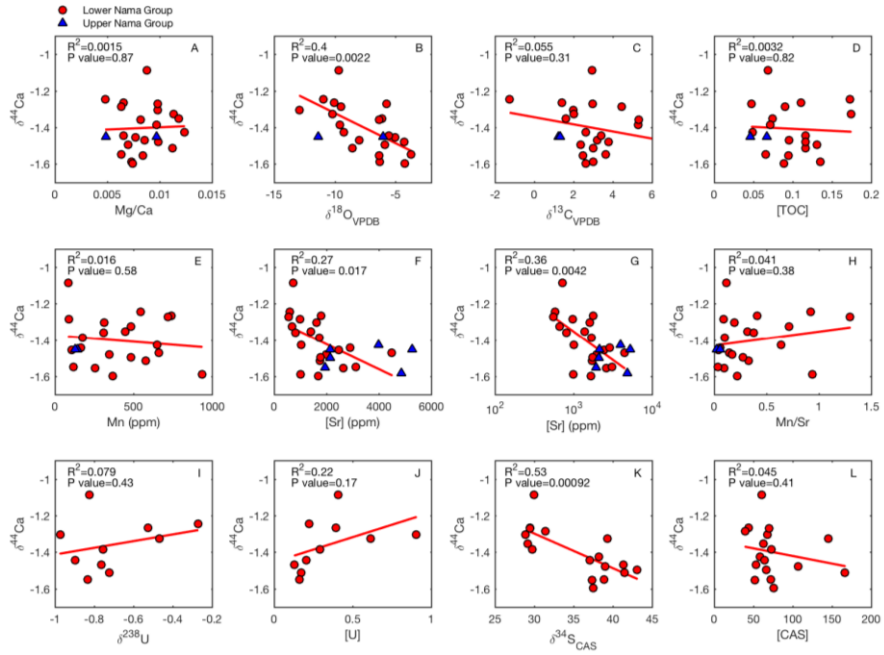

Figure 4: Cross plots of $\delta^{44}Ca$ against other geochemical parameters measured on the same samples. Red circles are from the Kuibis Subgroup, and blue triangles are from the Schwarzrand Subgroup. P-values and R^2 values for linear best fit lines are noted for the Kuibis Subgroup. Sr content is shown twice, once on a linear scale (F) and once on a log-linear scale (G).

Table 1: $\delta^{44}Ca$ data for each sample relative to modern seawater (SW), 915a (1.94‰ lower than SW), and BSE (0.94‰ lower than SW), along with the standard deviation (1σ) for the $\delta^{44}Ca$ data, and the strontium content.

Locality	*Sample name*	*Height (m)*	*$\delta^{44}Ca$ (SW)*	*$\delta^{44}Ca$ (915a)*	*$\delta^{44}Ca$ (BSE)*	*1σ*	*Sr content (ppm)*

Zebra River	LO2	4	−1.25	0.69	−0.31	0.065	590
	LO4	18	−1.30	0.64	−0.36	0.072	1617
	LO6	28	−1.27	0.67	−0.33	0.000	1794
	LO7	35	−1.33	0.61	−0.39	0.026	674
	LO11	44	−1.35	0.59	−0.41	0.055	1396
	OS2-3	75	−1.43	0.51	−0.49	0.025	1014
	OS2-4	85	−1.27	0.67	−0.33	0.050	555
	ZR5	106	−1.09	0.85	−0.15	0.026	730
	ZR9	122	−1.39	0.55	−0.45	0.063	1714
	OS2-9	131	−1.36	0.58	−0.42	0.046	818
	OS2-10	139	−1.46	0.48	−0.52	0.000	2452
	ZR18	152	−1.29	0.65	−0.35	0.105	979
	ZR31	173	−1.47	0.47	−0.53	0.019	4489
	ZR38	207	−1.44	0.50	−0.50	0.078	2892
	UH2	222	−1.59	0.35	−0.65	0.000	998
	UH4	231	−1.51	0.43	−0.57	0.007	1744
	UH5	236	−1.48	0.46	−0.54	0.069	1981
	UH6	242	−1.50	0.44	−0.56	0.000	1772
	UH8	254	−1.55	0.39	−0.61	0.032	2622
	UH9	259	−1.60	0.34	−0.66	0.000	1668
	UH14	285	−1.56	0.38	−0.62	0.000	
Pinnacle Reefs	PR7	5	−1.08	0.86	−0.14	0.013	
	PR	10	−1.07	0.87	−0.13	0.009	
	PR6	15	−1.39	0.55	−0.45	0.011	
Swartpunt	SW2	30	−1.45	0.49	−0.51	0.019	5270
	SW6	73	−1.58	0.36	−0.64	0.014	4845
	SW9	100	−1.43	0.51	−0.49	0.010	3973
	SW12	133	−1.50	0.44	−0.56	0.011	2128
	SW13	143	−1.55	0.39	−0.61	0.011	1936
	SWP15	153	−1.45	0.49	−0.51	0.134	2138

323

5. Discussion

The decrease of 0.35‰ in the calcium isotopic composition of carbonate rocks recorded through the Kuibis Subgroup is substantial, and of a similar magnitude to the change in $\delta^{44}Ca$ through the end-Ordovician mass extinction (0.5–0.6‰; Holmden et al., 2012), Cretaceous anoxic events (0.2–0.4‰; Blättler et al., 2011), and the Permo–Triassic Boundary (0.3‰; Payne et al., 2010). Following the progressive transition towards lower $\delta^{44}Ca$ across the Kuibis Subgroup, $\delta^{44}Ca$ remains low (around −1.5‰) throughout the Schwarzrand Subgroup, up to the Ediacaran–Cambrian Boundary.

A similar negative shift in $\delta^{44}Ca$ is recorded in contemporaneous rocks from South China (Sawaki et al., 2013), although those data come from five samples within a mixed dolomite and limestone succession, making it difficult to discern mineralogical controls from trends in seawater calcium isotopic composition. Pruss et al., (2018) report $\delta^{44}Ca$ from bulk rock samples from the Omkyk Member of the Nama Group that overlap with the range of $\delta^{44}Ca$ in this study (−1.07‰ to −1.59‰), but the $\delta^{44}Ca$ data come from fossil samples and are not presented stratigraphically. $\delta^{44}Ca$ data from the Wonoka Formation, deposited during the Shuram-Wonoka carbon isotope excursion, identify a prominent negative excursion, reaching from −0.8‰ to −1.9‰, before recovering to −0.8‰ (Husson et al., 2015). Dolomitised samples at the top of the Wonoka Formation may be contemporaneous with limestone samples at the base of the Nama Group, but the differing mineralogy makes it difficult to directly compare the $\delta^{44}Ca$ values.

Assuming the Nama Group has not experienced diagenetic alteration with fluid that has an exceptionally low $\delta^{44}Ca$ (Gussone et al., 2005), then the very low $\delta^{44}Ca$ recorded in the upper Kuibis and Schwarzrand subgroups can be interpreted to result from two

possible endmember scenarios: 1) local carbonate deposition associated with a larger local calcium isotopic fractionation ($\Delta^{44}Ca_{local}$) of around −1.7‰, in an ocean with a similar $\delta^{44}Ca_{SW}$ to today, or 2) local carbonate deposition associated with a smaller $\Delta^{44}Ca_{local}$ of around −1.25‰, in an ocean with $\delta^{44}Ca_{SW}$ that is 0.4–0.5‰ lower than today.

5.1 Scenario one: Preservation of local aragonite $\delta^{44}Ca$

In an ocean with a similar $\delta^{44}Ca$ to today, preservation of very low $\delta^{44}Ca$ (<−1.5‰) in carbonate rocks requires a large $\Delta^{44}Ca_{local}$ during carbonate mineral deposition (e.g., scenario 1). A local change from calcite towards aragonite deposition, or an increase in the precipitation rate of carbonate minerals, could drive changes in the Sr content and $\delta^{44}Ca$ of carbonate rocks in the direction and magnitude recorded across the Kuibis Subgroup (Figure 5a; Farkaš et al., 2016; Tang et al., 2008). It is likely that the original sedimentary mineralogies in the Nama Group were dominantly aragonite, consistent with petrographic work that has identified a dominantly aragonitic primary mineralogy for many, but not all, components including large botryoidal cements and crystal fans (Grant, 1990; Grotzinger et al., 2005; Wood et al., 2018).

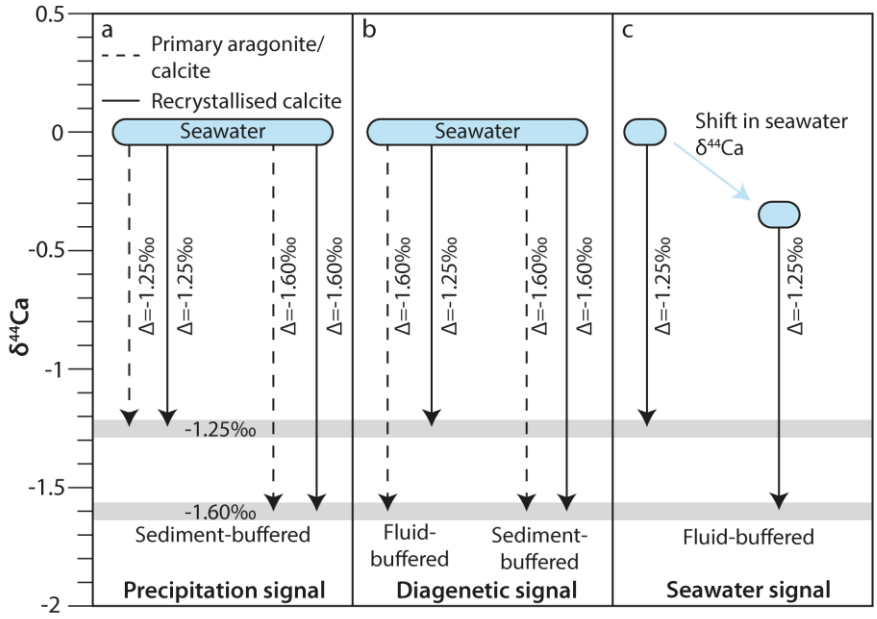

Figure 5: Schematic showing three possible models to explain the shift towards lower $\delta^{44}Ca$ across the Nama Group. Panel a) shows a change in fractionation during precipitation of primary minerals from seawater, resulting from either a change in mineralogy or precipitation rates, preserved in recrystallized calcite through sediment-buffered diagenesis. Panel b) shows a diagenetic interpretation, where the primary aragonite $\delta^{44}Ca$ is the same, but differences in $\delta^{44}Ca$ are introduced during recrystallisation to calcite under fluid- and sediment-buffered diagenesis (see section 5.1). Panel c) illustrates a change in seawater $\delta^{44}Ca$, which could be preserved in carbonate rocks during either fluid- or sediment-buffered diagenesis (see section 5.2).

During recrystallisation of primary aragonite to calcite, the $\delta^{44}Ca$ of the calcite is determined by the $\delta^{44}Ca$ of the pore fluid from which it precipitates. Under conditions of high fluid flow, pore fluids can be buffered by seawater Ca (fluid-buffered conditions). In contrast, when pore fluids become isolated from seawater, the $\delta^{44}Ca$ of the pore fluid can be buffered by the dissolution of the primary aragonite (sediment-buffered conditions) (Higgins et al., 2018). For primary aragonite $\delta^{44}Ca$ to be preserved it is thought that recrystallisation of the primary aragonite to calcite must occur under sediment-buffered conditions, such that the buried calcite should retain its primary aragonite $\delta^{44}Ca$. If instead, recrystallisation occurs under fluid-buffered conditions, the buried calcite can acquire a new $\delta^{44}Ca$ that reflects the smaller $\Delta^{44}Ca_{local}$ between newly precipitated calcite and the pore fluid (Ahm et al., 2018; Higgins et al., 2018) (Figure 5b).

Sedimentological, geochemical and fluid inclusion data suggest that the majority of primary carbonate minerals precipitating globally were aragonitic in the terminal Ediacaran (Brennan et al., 2004; Cui et al., 2019; Grotzinger et al., 2005; Zhuravlev and Wood, 2008). If aragonite is the dominant carbonate precipitate from the oceans globally, and if the buried carbonate minerals retain a low $\delta^{44}Ca$ during sediment-buffered recrystallisation, then more ^{40}Ca overall is removed from the ocean, and the $\delta^{44}Ca$ of the ocean should be higher (Blättler and Higgins, 2017). This increase in $\delta^{44}Ca_{sw}$ would mean that the $\delta^{44}Ca$ in carbonate rocks would be higher on average, as despite the large calcium isotopic fractionation factor, they are precipitating from a fluid with a higher $\delta^{44}Ca$. Certainly the carbonate minerals would on the whole be higher than the canonical value of −1.5‰ used to signify local primary aragonite deposition in the geological record (Higgins et al., 2018; Husson et al., 2015). It is therefore difficult to explain the very low $\delta^{44}Ca$

captured by some samples from the Nama Group as localized primary aragonite within a calcite-dominated ocean with the same $\delta^{44}Ca_{SW}$ as today. However, $\delta^{44}Ca_{SW}$ is determined by the final $\delta^{44}Ca$ of all buried carbonate, which may differ from the primary depositional $\delta^{44}Ca$, since primary depositional $\delta^{44}Ca$ may be reset as aragonite recrystallises to calcite. To explain very low $\delta^{44}Ca$ in ancient carbonate rocks requires *local* aragonite deposition and sediment-buffered $\delta^{44}Ca$ preservation within oceans where either 1) *globally*, the majority of primary carbonate minerals are deposited as calcite, or 2) *globally*, the majority of carbonate minerals are deposited as aragonite, but recrystallised to calcite or dolomite under fluid-buffered conditions.

If we interpret the shift in the $\delta^{44}Ca$ over the Nama Group as due entirely to local changes in the nature of recrystallization, i.e., in the style of diagenesis, then the shift to lower $\delta^{44}Ca$ across the Nama Group might record a local change towards recrystallisation under increasingly sediment-buffered conditions (Husson et al., 2015). This could be driven by higher sediment production and accumulation rates, which would push recrystallisation and neomorphism deeper into the sediment pile where it is not in as frequent contact with seawater. Higher burial rates could reflect a higher carbonate saturation state, or an overall marine transgressive succession that created accommodation space to fill with sediment more quickly. Importantly, this interpretation of the shift in $\delta^{44}Ca$ across the Nama Group would represent a local change in the preserved $\delta^{44}Ca$ that does not reflect changes in the global ocean, but could provide insight into local depositional conditions and diagenesis in the Nama Group.

One way to test whether the trend in $\delta^{44}Ca$ reflects local changes in fluid- vs. sediment-buffered diagenesis is to compare $\delta^{44}Ca$ with other geochemical proxies analysed

in the same samples. A transition from fluid-buffered to sediment-buffered diagenetic conditions should produce synchronous changes across multiple geochemical systems (Ahm et al., 2018; Higgins et al., 2018; Husson et al., 2015). For example, in the sulfur isotope system, recrystallisation of carbonate minerals during early diagenesis under fluid-buffered conditions may capture unaltered seawater $\delta^{34}S$, whereas recrystallisation in sediment-buffered conditions may capture an evolved pore fluid $\delta^{34}S$ (Rennie and Turchyn, 2014). In the Kuibis Subgroup, there is a weak but significant negative correlation between $\delta^{44}Ca$ and $\delta^{34}S_{CAS}$ ($P<0.05$, $R^2=0.53$; Figure 4k) that supports a change in the realm of diagenesis (sulfur isotope data from Tostevin et al., 2017). However, there is no significant correlation between $\delta^{44}Ca$ and carbonate-associated-sulfate (CAS) content (p-value =0.41), which should also be sensitive to fluid- vs. sediment-buffered recrystallisation, since CAS abundance is typically higher in calcite (10,000s of ppm) than in aragonite (1000s of ppm) (Busenberg and Plummer, 1985). Under sediment-buffered conditions, a decrease in CAS abundance would be expected as the sulfate concentration in the fluid would be set by the primary aragonite, but this is not observed.

We can also examine the relationship between $\delta^{44}Ca$ and uranium isotope data from the Kuibis Subgroup at Zebra River. In modern carbonate sediments, pore water reduction of uranium during early diagenesis offsets $\delta^{238}U$ in recrystallised carbonate minerals towards higher values (Chen et al., 2018). If recrystallisation takes place under deeper burial conditions, where the supply of uranium is limited, then the bulk carbonate sediment is more likely to retain a $\delta^{238}U$ close to primary seawater. Changes in the style of diagenesis should hence produce a positive correlation between $\delta^{44}Ca$ and $\delta^{238}U$. While in general, the higher $\delta^{44}Ca$ and $\delta^{238}U$ both occur in the Lower Omkyk Member, there is no

444 significant correlation between $\delta^{44}Ca$ and either $\delta^{238}U$ (p-value = 0.43) or U/Ca ratios (p-
445 value = 0.17; Figure 4i and 4j) measured on the same samples in the Kuibis Subgroup.
446 However, it is not clear whether this understanding of uranium isotope systematics,
447 developed in modern marine sediments, can be applied to sediments from an ocean with
448 widespread anoxia (Tostevin et al., 2019; Zhang et al., 2018).

449 During fluid-buffered diagenesis, the Sr content of carbonate rocks should be
450 reduced, reflecting the low abundance of Sr in calcite (1000 ppm). In contrast, sediment-
451 buffered diagenesis can conserve the original high Sr content associated with primary
452 aragonite precipitation (7000–9000 ppm) (Higgins et al., 2018). Changes in the primary
453 mineralogy or style of diagenesis should therefore result in a negative correlation between
454 $\delta^{44}Ca$ and the Sr content of carbonate rocks (Lau et al., 2017). Overall, there is a negative
455 correlation between strontium content and $\delta^{44}Ca$ in the Kuibis Subgroup at the $P < 0.05$
456 level that could support a diagenetic control, but with high scatter ($R^2=0.27$ for a linear
457 trend and $R^2=0.36$ for a log-linear trend). This trend is weak despite efforts to target
458 individual samples with a wide range of strontium contents, including those that are locally
459 anomalous compared to surrounding samples (Figures 2 and 4f). Further, in the
460 Schwarzrand Subgroup, Sr content in carbonate rocks declines, whereas $\delta^{44}Ca$ remains low
461 across the section.

462 In addition, changes in the style of diagenesis can be recorded in oxygen isotope
463 ratio, as $\delta^{18}O$ in carbonates decreases during recrystallisation at deeper burial depths.
464 Sediment-buffered recrystallisation could therefore result in lower $\delta^{18}O$ and lower $\delta^{44}Ca$
465 (Higgins et al., 2018). We find a weak correlation between $\delta^{44}Ca$ and $\delta^{18}O$ at the $P < 0.05$
466 level ($R^2=0.4$), but this is in the opposite direction than would be expected if these trends

were produced by changes in the style of diagenesis (Higgins et al., 2018; Husson et al., 2015). Such a relationship may be possible if sediment-buffered recrystallisation occurs in the presence of meteoric groundwaters, which can extend at depth below marine continental shelves. However, meteoric cements have not been noted in analysed samples in the Nama Group (Wood et al., 2018). In addition, there is no apparent correlation between $\delta^{44}Ca$ and $\delta^{13}C$ or TOC, or with other proxies that are partially impacted by changes in diagenetic conditions, such as Mn content, Mn/Sr, total iron (Fe_T) or Mg/Ca ratios (Figure 4a,e,h).

Times of high fluid flow driving fluid-buffered diagenesis could be expected to occur below sequence boundaries, but the $\delta^{44}Ca$ trend across the Nama Group cross cuts transgressive systems tracts, high stands and sequence boundaries, similar to $\delta^{44}Ca$ data in Triassic carbonate rocks (Lau et al., 2017) (Figure 2). This poses a further problem for the widespread interpretation of $\delta^{44}Ca$ in the geological record to only reflect fluid- vs. sediment-buffered recrystallisation. While local mineralogical and diagenetic controls provide a clear explanation for coupled geochemical trends recorded in modern carbonate sediments (Ahm et al., 2018; Higgins et al., 2018), as well as some ancient carbonate rocks (Ahm et al., 2019; Husson et al., 2015), a diagenetic framework for interpreting $\delta^{44}Ca$ can only partially explain the geochemical trends across the Nama Group. We suggest that while fluid- vs. sediment-buffered diagenesis is one important way to introduce variability into $\delta^{44}Ca$ measured in carbonate rocks, it may not be the only driver of change in the $\delta^{44}Ca$ of ancient carbonate rocks.

5.2 Scenario two: A change in seawater $\delta^{44}Ca$

An alternative suggestion is that the shift in $\delta^{44}Ca$ seen across the Nama Group represents a change in the global Ca cycle around ~550 Ma that lasted 11–14 Myrs (e.g., scenario 2; Figure 5c). Assuming there is no systematic change in primary carbonate mineralogy, mineral precipitation rates or diagenetic conditions across the Nama Group, we explore other ways to produce a negative shift in the $\delta^{44}Ca$ of carbonate rocks. The Late Ediacaran was a time of transformation, including new biological innovations, as well as profound changes in seawater chemistry, climate and style of sedimentation. The marine calcium cycle would likely have been sensitive to each of these changes. We will consider several of these in turn.

5.2.1 Evaporite deposition

The removal of calcium from the ocean is divided between carbonate mineral burial, evaporite mineral burial and minor sinks such as alteration of oceanic crust, which can fix calcium into the altered phases. Over long timescales, carbonate minerals are the dominant sink for calcium, and have a $\delta^{44}Ca$ similar to bulk silicate Earth (Blättler and Higgins, 2017). But during sporadic, geologically short-lived intervals of extensive evaporite deposition, the carbonate sink may form a smaller fraction of the total calcium sink. If enhanced evaporite deposition increases the proportion of calcium buried as $CaSO_4$, which typically has a similar $\delta^{44}Ca$ to seawater due to quantitative removal in evaporite basins (Blättler and Higgins, 2014), then the residual calcium isotope composition of seawater could decrease, through reduced removal of the ^{40}Ca isotope relative to ^{44}Ca. This shift in seawater $\delta^{44}Ca$ would be reflected in the $\delta^{44}Ca$ of carbonate minerals, and is consistent with the direction of the $\delta^{44}Ca$ shift across the Nama Group (Figure 5c).

513 Mass balance calculations suggest that an increase in the proportional evaporite
514 burial flux (the burial of Ca in evaporites as a proportion of the total Ca burial flux;
515 F_{evap}/F_{total}), can drive a decrease in seawater $\delta^{44}Ca$ (Figure 6 and Table 2). A 0.35‰
516 decrease in seawater $\delta^{44}Ca$ requires F_{evap}/F_{total} to increase from 2.5% to 37%. If the total
517 calcium burial flux remains fixed, at $1.4*10^{13}$ mols/year, then an F_{evap}/F_{total} of 37% equates
518 to an evaporite burial flux of $5.2*10^{12}$ mols/year. Even extensive evaporite deposition may
519 not generate sufficient calcium fluxes to account for the full magnitude of the $\delta^{44}Ca$ shift
520 (Hensley, 2006). However, when combined with other changes in the marine Ca cycle such
521 as a change in the style of dolomitisation, a smaller increase in evaporite burial is needed to
522 reconcile the change in $\delta^{44}Ca$ across the Nama Group.
523 Extensive evaporite deposition occurred in the late Ediacaran, evidenced by the
524 well-dated sulfate evaporites in Oman and possibly contemporaneous deposits along the
525 northern Gondwana margin in Pakistan, India, Iran and Australia (Claypool et al., 1980;
526 Houghton, 1980; Solomon et al., 1971; Strauss et al., 2001). Radiometric dates and sulfur
527 isotope chemostratigraphy place the deposition of the Kuibis Subgroup in the Nama Group
528 contemporaneous with the A0 Member of the Ara Group, in Oman (Bowring et al., 2007;
529 Fike and Grotzinger, 2008; Tostevin et al., 2017), which contains sulfate evaporite minerals,
530 providing a direct link between the timing of the $\delta^{44}Ca$ transition and evaporite deposition.
531 Calcite pseudomorphs after gypsum have been reported from the Dengying Formation,
532 South China, which is contemporaneous with the Nama Group (Cui et al., 2019; Duda et al.,
533 2016; Lu et al., 2013).
534

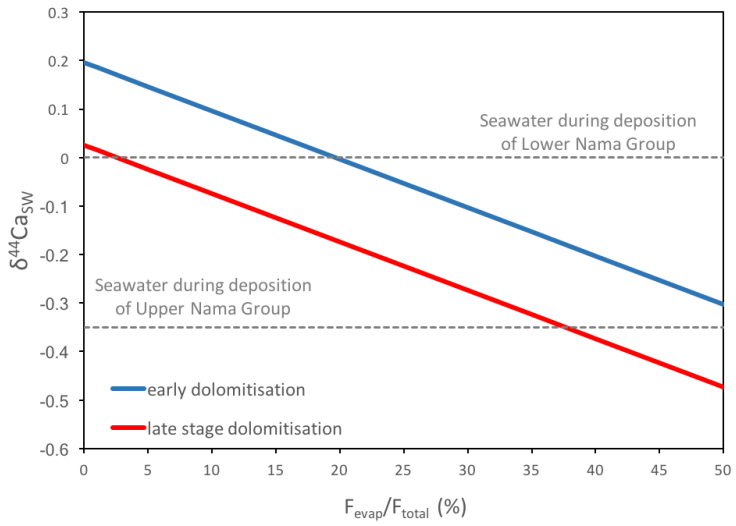

535

536 **Figure 6:** Steady-state mass balance model for seawater $\delta^{44}Ca$ as a function of the

537 proportional evaporite burial flux (F_{evap}/F_{total}). Two sets of calculations are shown, using a

538 $\Delta^{44}Ca$ for dolomitisation of either 0‰ (early dolomitisation; blue line) or –1.58‰ (late

539 stage dolomitisation; red line).

540

541 **Table 2:** Magnitude and $\delta^{44}Ca$ of fluxes used in evaporite mass balance cycle model.

542 The model assumes that the input fluxes are equal to the output fluxes (i.e., steady state).

	Flux	**Magnitude**	**$\delta^{44}Ca$ (‰)**
Inputs	Riverine	$1.24*10^{13}$	–1.08
	Dolomitisation	$1.5*10^{12}$	–1.58 (late-stage)
			0 (early)
Outputs	Limestone	$(1–F_{evap})$	–1.3 (average)
	Evaporite	F_{evap} (varied from 0 to	-0.18

		100%)	
	Alteration of oceanic crust	$1.5*10^{12}$	= seawater

543

544

545 **5.2.2 Enhanced continental weathering**

546 Enhanced continental weathering could drive an increase in the delivery of calcium
547 to seawater. If there is an imbalance between the riverine Ca flux, and the carbonate
548 sedimentation flux, both the concentration and isotopic ratio of calcium in seawater can be
549 perturbed. For example, a 300% increase in the riverine Ca flux can produce a 0.2–0.4‰
550 negative calcium isotope excursion in seawater over 0.5–1 Myrs (Blättler et al., 2011),
551 which is comparable in magnitude to the progressive 0.35‰ decline in $\delta^{44}Ca$ across the
552 Nama Group, although over the longer timescale of 11–14 million years. Given the
553 residence time of calcium in seawater (1.1 Myrs in the modern ocean), it is difficult to
554 sustain an isotopic perturbation over such long timescales, because carbonate precipitation
555 rates would rise in response to higher marine calcium concentrations, driving seawater
556 $\delta^{44}Ca$ back towards higher values.

557 Enhanced continental weathering is supported by the rise in Sr content across the
558 Nama Group. Strontium contents in carbonates are partially controlled by the size of the
559 seawater Sr reservoir, which is also sensitive to the mass balance between continental
560 weathering and carbonate deposition (Steuber and Veizer, 2002). Although the Sr content
561 of carbonate rocks is partially controlled by precipitation rate, mineralogy, and diagenesis,
562 global variations in the Sr content of carbonate rocks across multiple sections implies

563 secular variation in the size of the marine Sr reservoir. A rise in strontium content through
564 the Kuibis Subgroup is recorded independently in four sections in this study, as well as in
565 previous studies of the Nama Group (Ries et al., 2009), despite the different extraction
566 method used. A similar rise in Sr content been reported globally in the contemporaneous
567 carbonate rocks from the Dengying Formation, south China (Cui et al., 2016b) and the
568 Bambui Formation, Brazil (Caetano-Filho et al., 2019). This supports a secular change in
569 the size of the seawater Sr reservoir consistent with enhanced continental weathering.
570
571 **5.2.3 Changes in the style of dolomitisation**
572 Over long timescales, the average carbonate depositional sink must be close to bulk
573 silicate Earth, although within this bulk carbonate sink, dolomite tends towards higher
574 $\delta^{44}Ca$ and limestone towards lower $\delta^{44}Ca$ (Blättler and Higgins, 2017). Therefore, any
575 changes in the amount of dolomite, or the calcium isotopic fractionation associated with
576 dolomitisation, could influence the $\delta^{44}Ca$ of seawater, and hence the average $\delta^{44}Ca$ of
577 limestone deposition. A switch from early dolomitisation, where dolomite retains the low
578 $\delta^{44}Ca$ associated with primary aragonite or calcite, towards late-stage dolomitisation,
579 where the $\delta^{44}Ca$ is re-set and ^{40}Ca is preferentially released into pore fluids, could result in
580 a decrease in seawater $\delta^{44}Ca$ of up to 0.17‰ (Table 2 and Figure 6).
581 In Neogene environments, dolomite commonly has a higher $\delta^{44}Ca$ than limestone
582 (Blättler et al., 2015; Fantle and Higgins, 2014; Higgins et al., 2018). In contrast, such
583 differences are not visible in compilations of carbonate rocks across the Precambrian (from
584 3.0 – 0.7 Ga; Blättler and Higgins, 2017). Early marine cements from carbonate rocks on the
585 Siberian Platform support a fundamental transition in the carbonate system in the Late

586 Ediacaran, from “aragonite-dolomite” seas to “aragonite” seas (Wood et al., 2017b),
587 possibly driven by a reduction in the seawater Mg/Ca ratio. It is possible that the late
588 Ediacaran captures a transition in the style of dolomitisation, from early mimetic
589 dolomitisation, with a similar $\delta^{44}Ca$ to limestone, towards later stage “Phanerozoic style”
590 dolomitisation with a higher $\delta^{44}Ca$ (Blättler et al., 2015; Fantle and Higgins, 2014). This
591 would drive a decrease in the average $\delta^{44}Ca$ seawater, which would be reflected in the
592 lower $\delta^{44}Ca$ captured by marine limestones.
593
594 **5.2.4 Additional evidence for changes in Ediacaran seawater chemistry**
595 The negative shift in $\delta^{44}Ca$ across the Nama Group may result from a combination of
596 environmental factors. For example, the rapid change in $\delta^{44}Ca$ across the Kuibis Subgroup
597 may reflect an imbalance in the calcium cycle during the onset of higher continental
598 weathering rates, resulting in the growth of the marine calcium and sulfate reservoirs, and
599 thus a reduction in the seawater Mg/Ca ratio. The system could then have reached a new
600 steady state in the Schwarzrand Subgroup; with higher weathering rates matched by
601 increased carbonate and evaporite deposition, and changes in the style of dolomitisation.
602 Evaporite deposition could further decrease marine Mg/Ca ratios, as the burial flux of Mg
603 in evaporite deposits, as a proportion of the total Mg budget, is larger than the proportional
604 burial flux of Ca. Increased physical and chemical weathering would impact multiple
605 biogeochemical cycles, delivering Ca, Sr and SO_4^{2-} ions, alkalinity, and nutrients to the
606 oceans (Blättler et al., 2011).
607 An increase in marine calcium concentrations across the Ediacaran–Cambrian
608 boundary is supported by evidence for a peak in physical and chemical weathering of

609 continental crust in long-term stratigraphic and geochemical records (Peters and Gaines,
610 2012). For example, very high $^{87}Sr/^{86}Sr$ (from 0.708 to 0.7087) are recorded in Late
611 Ediacaran limestones from South China (Figure 7a), Mongolia (Figure 7b), Oman (Figure
612 7c), Namibia, (Figure 7d) and Siberia (Figure 7e), interpreted to reflect enhanced
613 continental weathering (Brasier et al., 1996; Burns et al., 1994; Cui et al., 2016a, 2015;
614 Kaufman et al., 1993; Sawaki et al., 2013). Although there is some variability in the
615 $^{87}Sr/^{86}Sr$ ratio between sections, the high values are consistent with long term
616 compilations that show $^{87}Sr/^{86}Sr$ reached a peak during the late Ediacaran (Halverson et
617 al., 2007). An expansion of seafloor anoxia, recorded by uranium and sulfur isotopes, could
618 be a response to elevated nutrient input (Figure 8) (Tostevin et al., 2019; Zhang et al.,
619 2018). Enhanced delivery of sulfate could also drive a rise in pyrite burial, as well as
620 changes in riverine $\delta^{34}S$, and could be consistent with $\delta^{34}S_{CAS}$ and $\Delta^{33}S_{CAS}$ records from the
621 Nama and Ara groups (Figure 8) (Fike and Grotzinger, 2008; Tostevin et al., 2017; Wu et al.,
622 2015). Thus many geochemical proxies have been suggested to reflect some change in
623 terrestrial weathering over this interval.
624

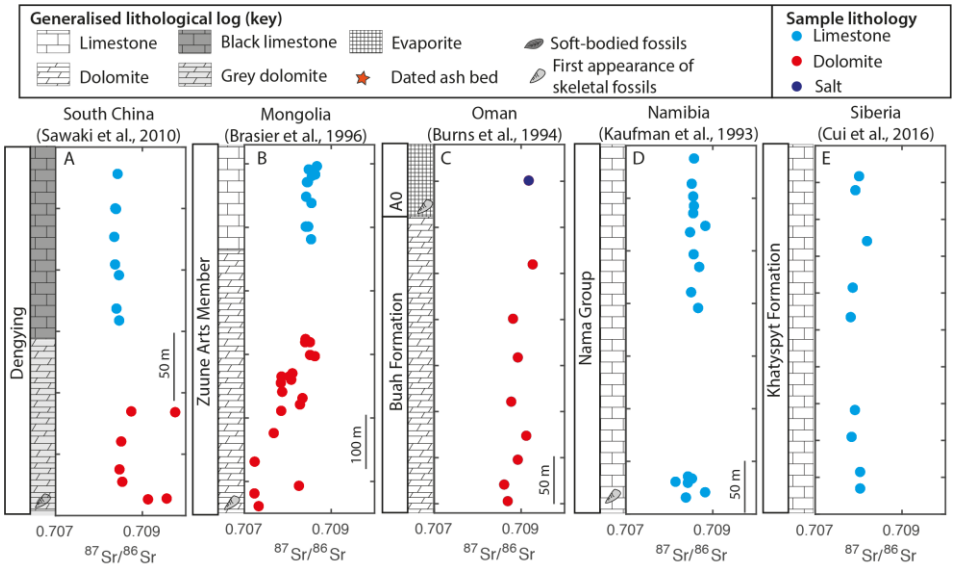

625

626 **Figure 7**: $^{87}Sr/^{86}Sr$ ratios for the last ca. 10 Myr of the terminal Ediacaran, compiled from
627 the literature. $^{87}Sr/^{86}Sr$ from south China are from the Dengying formation (Sawaki et al.,
628 2010). $^{87}Sr/^{86}Sr$ from Mongolia were reported from the Tsagaan Oloom Formation (Brasier
629 et al., 1996), and subsequent stratigraphic revisions place the data in the late Ediacaran
630 Zuune Arts Member (Macdonald et al., 2009). Data from Oman are from the Buah and Ara
631 Formations (Burns et al., 1994). Data from the Nama Group are from Kaufman et al.,
632 (1993). Data from the Khatyspyt Formation are from (Cui et al., 2016a).

633

Commented [RT1]: Petach, works with Emmy smith.
Zuune arts formation

Remove Mongolia
No fossils

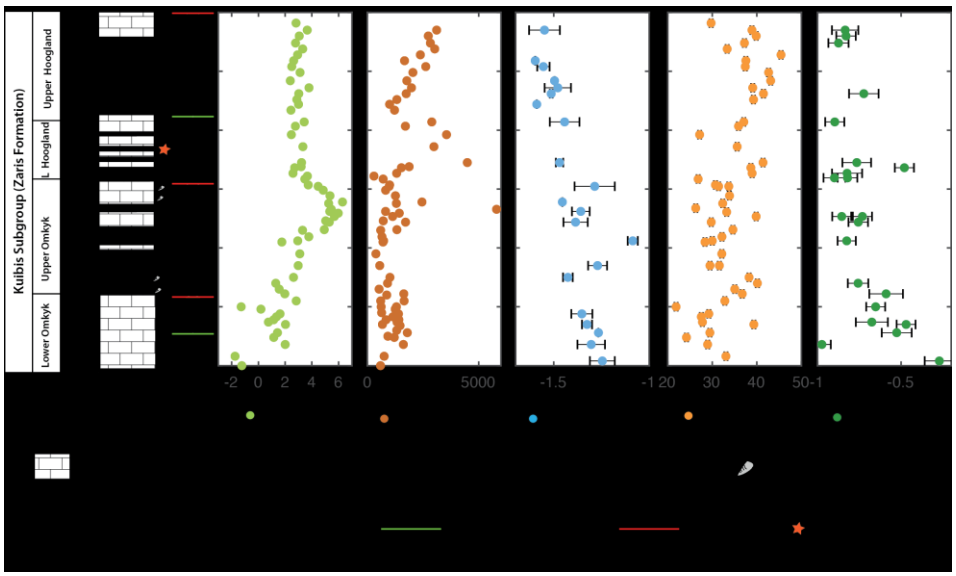

Figure 8: From left to right: Stratigraphic log, sequence stratigraphy, carbon isotope data, Sr content, $\delta^{44}Ca$, $\delta^{34}S_{CAS}$ and $\delta^{238}U$ for the Lower Nama Group at Zebra River Farm. Beds containing skeletal fossils are marked on the stratigraphic log. $\delta^{238}U$ and $\delta^{34}S_{CAS}$ data are published in full in Tostevin et al., 2019 and 2017, respectively. Sequence stratigraphy is from Adams et al., (2005)

Increased calcium concentrations, and an associated reduction in the seawater Mg/Ca ratio, would increase the carbonate saturation state and alter the stability of various carbonate precipitates. High carbonate saturation states are consistent with a dominance of carbonate lithologies, associated with exceptionally high accumulation rates (~65 m/Myr in the Dengying Formation, and ~100 m/Myr in the Nama Group) (Cui et al., 2016b), as well as densely-aggregating reefs with extensive synsedimentary cement, large meter-scale metazoans, and *Suvorovella* shells beds >1 km in length (Cai et al., 2011;

Grotzinger et al., 2005; Penny et al., 2014; Wood et al., 2017a, 2002; Wood and Curtis, 2015). This may have been driven by increasing marine calcium concentrations, although the onset of bioturbation around ~560 Ma may also have contributed to increased carbonate saturation, by modifying pH gradients in the top centimetres of sediment and returning sediment alkalinity to bottom waters (Higgins et al., 2009).

Despite a proposed increase in sulfate and calcium delivery to the oceans, seawater would likely have remained below critical supersaturation with respect to gypsum. Evaporite deposition is instead controlled by tectonic and climatic factors, such as the formation of semi-isolated basins during rifting. The assembly of Gondwana, between ~580 and ~550 Ma, was associated with tectonic inversion and the weathering of Tonian age evaporite deposits (Shields et al., 2019). The end of this period may have marked a slow-down in evaporite weathering, ushering in a new period of rifting and evaporite deposition. The rifting of the proposed supercontinent Pannotia may have occurred around this time, although the existence of this short-lived supercontinent is debated (Scotese, 2009). Together, geological, sedimentological and geochemical evidence supports higher rates of continental weathering, sustained over tens of millions of years, which delivered sulfate and calcium ions to Late Ediacaran oceans.

5.3 Implications for early skeletal animals

Calcareous hard parts appeared relatively abruptly in the terminal Ediacaran (~550 Ma) in a range of immobile, shallow marine benthos of probable diverse affinity (Wood, 2011). These early skeletal taxa are found exclusively in carbonate settings and likely formed biominerals via a pre-existing organic matrix. Together, these observations suggest

671 that the earliest calcification occurred preferentially in $CaCO_3$ saturated waters (Wood et
672 al., 2017a). Biomineralisation is energetically costly (Knoll, 2003), and the impetus for its
673 development in the terminal Ediacaran remains enigmatic.

674 If the shift in $\delta^{44}Ca$ records enhanced continental weathering and delivery of
675 calcium ions, the apparent coincidence in time with the first appearance of skeletal animals
676 may be significant for three reasons. Firstly, high carbonate saturation in shallow shelf
677 environments could have facilitated the onset of passive calcification (Wood et al., 2017a).
678 Secondly, under high seawater calcium concentrations, cellular transporters may struggle
679 to regulate intracellular calcium levels, which can lead to calcium toxicity (Simkiss, 1977).
680 In response, organisms may begin to precipitate carbonate minerals as a mechanism to
681 effectively expel calcium from the cell. Thirdly, a reduction in the Mg/Ca ratio of the ocean
682 would have thermodynamically favoured widespread aragonite precipitation over
683 dolomite (Wood et al., 2017). No organism is known to co-opt dolomite as a biomineral, but
684 most Ediacaran skeletal metazoans formed their shells from aragonite (Zhuravlev and
685 Wood, 2008).

686 While environmental changes may have contributed to the appearance of calcareous
687 skeletons, by making options evolutionarily available that were previously inaccessible, the
688 primary factor explaining the appearance of biomineralisation must be ecological (Vermeij,
689 1989; Wood, 2011). Biomineralisation was preceded by the appearance of motility (~560
690 Ma) and possible carnivory (~550 Ma), and the development of hard parts would have
691 been beneficial for the protection of soft tissue (Knoll, 2003). However, it is possible that
692 environmental changes made building aragonitic skeletons progressively more favourable
693 after ~550 Ma.

6. Conclusions

We present new $\delta^{44}Ca$ data for limestone rocks from the Nama Group, Namibia, that reveal a shift towards lower $\delta^{44}Ca$ around ~550 Ma. One interpretation of this shift is a local change from fluid- to sediment-buffered diagenesis of primary aragonite deposited over this interval. However, this interpretation is difficult to reconcile with changes in other geochemical and sequence stratigraphic records from the Nama Group that change across independent timescales. If instead, $\delta^{44}Ca$ records changes in the marine calcium cycle, the data could indicate enhanced weathering fluxes, matched by increased evaporite deposition and changes in the style of carbonate deposition. Enhanced weathering would also deliver more SO_4^{2-}, alkalinity and nutrients to the oceans, and this is supported in the late Ediacaran by an array of stratigraphic, sedimentological and geochemical records. Increased marine calcium concentrations, and lower Mg/Ca ratios (<5) could have facilitated the appearance of aragonitic skeletal animals, which are documented from within the same successions.

Acknowledgements

RT, GAS and RAW acknowledge financial support from NERC's Life and the Planet project (NE/1005978/1). We are grateful to L. and G. Fourie for access to Zebra River farm, and L. G' Evereet for access to Swartpunt Farm. We thank Helke Mocke from the Namibian Geological Survey, and Gerd Winterleitner assisted with field work.

References

717 Adams, E.W., Grotzinger, J.P., Watters, W.A., Schroder, S., McCormick, D.S., Al-Siyabi, H.A.,
718 2005. Digital characterization of thrombolite-stromatolite reef distribution in a
719 carbonate ramp system (terminal Proterozoic, Nama Group, Namibia). AAPG Bull. 89,
720 1293–1318. https://doi.org/10.1306/06160505005
721 Ahm, A.-S.C., Bjerrum, C.J., Blättler, C.L., Swart, P.K., Higgins, J.A., 2018. Quantifying early
722 marine diagenesis in shallow-water carbonate sediments. Geochim. Cosmochim. Acta,
723 Chemistry of oceans past and present: A Special Issue in tribute to Harry Elderfield 236,
724 140–159. https://doi.org/10.1016/j.gca.2018.02.042
725 Ahm, A.-S.C., Maloof, A.C., Macdonald, F.A., Hoffman, P.F., Bjerrum, C.J., Bold, U., Rose, C.V.,
726 Strauss, J.V., Higgins, J.A., 2019. An early diagenetic deglacial origin for basal Ediacaran
727 "cap dolostones." Earth Planet. Sci. Lett. 506, 292–307.
728 https://doi.org/10.1016/j.epsl.2018.10.046
729 Bjerrum, C.J., Canfield, D.E., 2011. Towards a quantitative understanding of the late
730 Neoproterozoic carbon cycle. Proc. Natl. Acad. Sci. 108, 5542–5547.
731 https://doi.org/10.1073/pnas.1101755108
732 Blättler, C.L., Henderson, G.M., Jenkyns, H.C., 2012. Explaining the Phanerozoic Ca isotope
733 history of seawater. Geology 40, 843–846. https://doi.org/10.1130/G33191.1
734 Blättler, C.L., Higgins, J.A., 2017. Testing Urey's carbonate–silicate cycle using the calcium
735 isotopic composition of sedimentary carbonates. Earth Planet. Sci. Lett. 479, 241–251.
736 https://doi.org/10.1016/j.epsl.2017.09.033
737 Blättler, C.L., Higgins, J.A., 2014. Calcium isotopes in evaporites record variations in Phanerozoic
738 seawater SO4 and Ca. Geology G35721–1.
739 Blättler, C.L., Jenkyns, H.C., Reynard, L.M., Henderson, G.M., 2011. Significant increases in
740 global weathering during Oceanic Anoxic Events 1a and 2 indicated by calcium isotopes.
741 Earth Planet. Sci. Lett. 309, 77–88. https://doi.org/10.1016/j.epsl.2011.06.029
742 Blättler, C.L., Miller, N.R., Higgins, J.A., 2015. Mg and Ca isotope signatures of authigenic
743 dolomite in siliceous deep-sea sediments. Earth Planet. Sci. Lett. 419, 32–42.
744 https://doi.org/10.1016/j.epsl.2015.03.006
745 Bowring, S.A., Grotzinger, J.P., Condon, D.J., Ramezani, J., Newall, M.J., Allen, P.A., 2007.
746 Geochronologic constraints on the chronostratigraphic framework of the
747 Neoproterozoic Huqf Supergroup, Sultanate of Oman. Am. J. Sci. 307, 1097–1145.
748 https://doi.org/10.2475/10.2007.01
749 Bowyer, F., Wood, R.A., Poulton, S.W., 2017. Controls on the evolution of Ediacaran metazoan
750 ecosystems: A redox perspective. Geobiology 15, 516–551.
751 https://doi.org/10.1111/gbi.12232
752 Bradbury, H.J., Torfstein, A., Wong, K., Turchyn, A.V., 2018. The Calcium Isotope Systematics of
753 the Late Quaternary Dead Sea Basin Lakes. Geochem. Geophys. Geosystems 19, 4260–
754 4273. https://doi.org/10.1029/2018GC007898
755 Bradbury, H.J., Turchyn, A.V., 2018. Calcium isotope fractionation in sedimentary pore fluids
756 from ODP Leg 175: Resolving carbonate recrystallization. Geochim. Cosmochim. Acta,
757 Chemistry of oceans past and present: A Special Issue in tribute to Harry Elderfield 236,
758 121–139. https://doi.org/10.1016/j.gca.2018.01.040
759 Brasier, M.D., Shields, G., Kuleshov, V.N., Zhegallo, E.A., 1996. Integrated Chemo- and
760 Biostratigraphic Calibration of Early Animal Evolution: Neoproterozoic–Early Cambrian

761 of Southwest Mongolia. Geol. Mag. 133, 445–485.
762 https://doi.org/10.1017/S0016756800007603
763 Brennan, S.T., Lowenstein, T.K., Horita, J., 2004. Seawater chemistry and the advent of
764 biocalcification. Geology 32, 473–476. https://doi.org/10.1130/G20251.1
765 Burns, S.J., Haudenschild, U., Matter, A., 1994. The strontium isotopic composition of
766 carbonates from the late Precambrian (~ 560-540 Ma) Huqf Group of Oman. Chem.
767 Geol. 111, 269–282. https://doi.org/10.1016/0009-2541(94)90094-9
768 Busenberg, E., Plummer, L.N., 1985. Kinetic and thermodynamic factors controlling the
769 distribution of SO 32- and Na + in calcites and selected aragonites. Geochim.
770 Cosmochim. Acta 49, 713–725. https://doi.org/10.1016/0016-7037(85)90166-8
771 Caetano-Filho, S., Paula-Santos, G.M., Guacaneme, C., Babinski, M., Bedoya-Rueda, C., Peloso,
772 M., Amorim, K., Afonso, J., Kuchenbecker, M., Reis, H.L.S., Trindade, R.I.F., 2019.
773 Sequence stratigraphy and chemostratigraphy of an Ediacaran-Cambrian foreland-
774 related carbonate ramp (Bambuí Group, Brazil). Precambrian Res. 331, 105365.
775 https://doi.org/10.1016/j.precamres.2019.105365
776 Cai, Y., Schiffbauer, J.D., Hua, H., Xiao, S., 2011. Morphology and paleoecology of the late
777 Ediacaran tubular fossil Conotubus hemiannulatus from the Gaojiashan Lagerstätte of
778 southern Shaanxi Province, South China. Precambrian Res. 191, 46–57.
779 https://doi.org/10.1016/j.precamres.2011.09.002
780 Chen, X., Romaniello, S.J., Herrmann, A.D., Hardisty, D., Gill, B.C., Anbar, A.D., 2018. Diagenetic
781 effects on uranium isotope fractionation in carbonate sediments from the Bahamas.
782 Geochim. Cosmochim. Acta 237, 294–311. https://doi.org/10.1016/j.gca.2018.06.026
783 Claypool, G.E., Holser, W.T., Kaplan, I.R., Sakai, H., Zak, I., 1980. The age curves of sulfur and
784 oxygen isotopes in marine sulfate and their mutual interpretation. Chem. Geol. 28, 199–
785 260. https://doi.org/10.1016/0009-2541(80)90047-9
786 Cui, H., Grazhdankin, D.V., Xiao, S., Peek, S., Rogov, V.I., Bykova, N.V., Sievers, N.E., Liu, X.-M.,
787 Kaufman, A.J., 2016a. Redox-dependent distribution of early macro-organisms: Evidence
788 from the terminal Ediacaran Khatyspyt Formation in Arctic Siberia. Palaeogeogr.
789 Palaeoclimatol. Palaeoecol. 461, 122–139.
790 https://doi.org/10.1016/j.palaeo.2016.08.015
791 Cui, H., Kaufman, A.J., Xiao, S., Peek, S., Cao, H., Min, X., Cai, Y., Siegel, Z., Liu, X.-M., Peng, Y.,
792 Schiffbauer, J.D., Martin, A.J., 2016b. Environmental context for the terminal Ediacaran
793 biomineralization of animals. Geobiology. https://doi.org/10.1111/gbi.12178
794 Cui, H., Kaufman, A.J., Xiao, S., Zhou, C., Liu, X.-M., 2017. Was the Ediacaran Shuram Excursion a
795 globally synchronized early diagenetic event? Insights from methane-derived authigenic
796 carbonates in the uppermost Doushantuo Formation, South China. Chem. Geol. 450,
797 59–80. https://doi.org/10.1016/j.chemgeo.2016.12.010
798 Cui, H., Kaufman, A.J., Xiao, S., Zhu, M., Zhou, C., Liu, X.-M., 2015. Redox architecture of an
799 Ediacaran ocean margin: Integrated chemostratigraphic (δ13C–δ34S–87Sr/86Sr–Ce/Ce*)
800 correlation of the Doushantuo Formation, South China. Chem. Geol. 405, 48–62.
801 https://doi.org/10.1016/j.chemgeo.2015.04.009

802 Cui, H., Xiao, S., Cai, Y., Peek, S., Plummer, R.E., Kaufman, A.J., 2019. Sedimentology and
803 chemostratigraphy of the terminal Ediacaran Dengying Formation at the Gaojiashan
804 section, South China. Geol. Mag. 1–25. https://doi.org/10.1017/S0016756819000293
805 Derry, L.A., 2010. A burial diagenesis origin for the Ediacaran Shuram-Wonoka carbon isotope
806 anomaly. Earth Planet. Sci. Lett. 294, 152–162.
807 Duda, J.-P., Zhu, M., Reitner, J., 2016. Depositional dynamics of a bituminous carbonate facies in
808 a tectonically induced intra-platform basin: the Shibantan Member (Dengying
809 Formation, Ediacaran Period). Carbonates Evaporites 31, 87–99.
810 https://doi.org/10.1007/s13146-015-0243-8
811 Fantle, M.S., DePaolo, D.J., 2007. Ca isotopes in carbonate sediment and pore fluid from ODP
812 Site 807A: The Ca2+(aq)–calcite equilibrium fractionation factor and calcite
813 recrystallization rates in Pleistocene sediments. Geochim. Cosmochim. Acta 71, 2524–
814 2546. https://doi.org/10.1016/j.gca.2007.03.006
815 Fantle, M.S., Higgins, J., 2014. The effects of diagenesis and dolomitization on Ca and Mg
816 isotopes in marine platform carbonates: Implications for the geochemical cycles of Ca
817 and Mg. Geochim. Cosmochim. Acta 142, 458–481.
818 https://doi.org/10.1016/j.gca.2014.07.025
819 Farkaš, J., Frýda, J., Holmden, C., 2016. Calcium isotope constraints on the marine carbon cycle
820 and CaCO3 deposition during the late Silurian (Ludfordian) positive δ13C excursion.
821 Earth Planet. Sci. Lett. 451, 31–40. https://doi.org/10.1016/j.epsl.2016.06.038
822 Fike, D.A., Grotzinger, J.P., 2008. A paired sulfate–pyrite δ34S approach to understanding the
823 evolution of the Ediacaran–Cambrian sulfur cycle. Geochim. Cosmochim. Acta 72, 2636–
824 2648. https://doi.org/10.1016/j.gca.2008.03.021
825 Germs, G.J.B., 1974. The Nama Group in South West Africa and Its Relationship to the Pan-
826 African Geosyncline. J. Geol. 82, 301–317.
827 Germs, G.J.B., 1972. New shelly fossils from Nama Group, South West Africa. Am. J. Sci. 272,
828 752–761. https://doi.org/10.2475/ajs.272.8.752
829 Grant, S.W., 1990. Shell structure and distribution of Cloudina, a potential index fossil for the
830 terminal Proterozoic. Am. J. Sci. 290-A, 261–294.
831 Grotzinger, J.P., Adams, E.W., Schroder, S., 2005. Microbial–metazoan reefs of the terminal
832 Proterozoic Nama Group (c. 550–543 Ma), Namibia. Geol. Mag. 142, 499–517.
833 Grotzinger, J.P., Bowring, S.A., Saylor, B.Z., Kaufman, A.J., 1995. Biostratigraphic and
834 Geochronologic Constraints on Early Animal Evolution. Science 270, 598–604.
835 Grotzinger, J.P., James, N.P., 2000. Carbonate sedimentation and diagenesis in the evolving
836 Precambrian world. SEPM.
837 Grotzinger, J.P., Watters, W.A., Knoll, A.H., 2000. Calcified metazoans in thrombolite-
838 stromatolite reefs of the terminal Proterozoic Nama Group, Namibia. Paleobiology 26,
839 334–359.
840 Gussone, N., Bohm, F., Eisenhauer, A., Dietzel, M., Heuser, A., Teichert, B., Reitner, J.,
841 Worheide, G., Dullo, W.-C., 2005. Calcium isotope fractionation in calcite and aragonite.
842 Geochim. Cosmochim. Acta 69, 4485–4494.
843 Halverson, G.P., Dudás, F.Ö., Maloof, A.C., Bowring, S.A., 2007. Evolution of the 87Sr/86Sr
844 composition of Neoproterozoic seawater. Palaeogeogr. Palaeoclimatol. Palaeoecol.,

Neoproterozoic to Paleozoic Ocean Chemistry 256, 103–129. https://doi.org/10.1016/j.palaeo.2007.02.028
Hensley, T.M., 2006. Calcium Isotopic Variation in Marine Evaporites and Carbonates: Applications to Late Miocene Mediterranean Brine Chemistry and Late Cenozoic Calcium Cycling in the Oceans.
Higgins, J.A., Blättler, C.L., Lundstrom, E.A., Santiago-Ramos, D.P., Akhtar, A.A., Crüger Ahm, A.-S., Bialik, O., Holmden, C., Bradbury, H., Murray, S.T., Swart, P.K., 2018. Mineralogy, early marine diagenesis, and the chemistry of shallow-water carbonate sediments. Geochim. Cosmochim. Acta 220, 512–534. https://doi.org/10.1016/j.gca.2017.09.046
Higgins, J.A., Fischer, W.W., Schrag, D.P., 2009. Oxygenation of the ocean and sediments: Consequences for the seafloor carbonate factory. Earth Planet. Sci. Lett. 284, 25–33. https://doi.org/10.1016/j.epsl.2009.03.039
Hinojosa, J.L., Brown, S.T., Chen, J., DePaolo, D.J., Paytan, A., Shen, S., Payne, J.L., 2012. Evidence for end-Permian ocean acidification from calcium isotopes in biogenic apatite. Geology 40, 743–746. https://doi.org/10.1130/G33048.1
Holmden, C., Panchuk, K., Finney, S.C., 2012. Tightly coupled records of Ca and C isotope changes during the Hirnantian glaciation event in an epeiric sea setting. Geochim. Cosmochim. Acta 98, 94–106. https://doi.org/10.1016/j.gca.2012.09.017
Houghton, M.L., 1980. Geochemistry of the Proterozoic Hormuz Evaporites, Southern Iran. University of Oregon.
Husson, J.M., Higgins, J.A., Maloof, A.C., Schoene, B., 2015. Ca and Mg isotope constraints on the origin of Earth's deepest C excursion. Geochim. Cosmochim. Acta 160, 243–266. https://doi.org/10.1016/j.gca.2015.03.012
Jensen, S., Runnegar, B.N., 2005. A complex trace fossil from the Spitskop Member (terminal Ediacaran–? Lower Cambrian) of southern Namibia. Geol. Mag. 142, 561–569.
Jensen, S., Saylor, B.Z., Gehling, J.G., Germs, G.J.B., 2000. Complex trace fossils from the terminal Proterozoic of Namibia. Geology 28, 143–146.
Kaufman, A.J., Hayes, J., Knoll, A.H., Germs, G.J., 1991. Isotopic compositions of carbonates and organic carbon from upper Proterozoic successions in Namibia: stratigraphic variation and the effects of diagenesis and metamorphism. Precambrian Res. 49, 301–327.
Kaufman, A.J., Jacobsen, S.B., Knoll, A.H., 1993. The Vendian record of Sr and C isotopic variations in seawater: Implications for tectonics and paleoclimate. Earth Planet. Sci. Lett. 120, 409–430. https://doi.org/10.1016/0012-821X(93)90254-7
Knauth, L.P., Kennedy, M.J., 2009. The late Precambrian greening of the Earth. Nature 460, 728–732.
Knoll, A.H., 2003. Biomineralization and Evolutionary History. Rev. Mineral. Geochem. 54, 329–356. https://doi.org/10.2113/0540329
Lau, K.V., Maher, K., Brown, S.T., Jost, A.B., Altıner, D., DePaolo, D.J., Eisenhauer, A., Kelley, B.M., Lehrmann, D.J., Paytan, A., Yu, M., Silva-Tamayo, J.C., Payne, J.L., 2017. The influence of seawater carbonate chemistry, mineralogy, and diagenesis on calcium isotope variations in Lower-Middle Triassic carbonate rocks. Chem. Geol. 471, 13–37. https://doi.org/10.1016/j.chemgeo.2017.09.006
Linnemann, U., Ovtcharova, M., Schaltegger, U., Gärtner, A., Hautmann, M., Geyer, G., Vickers-Rich, P., Rich, T., Plessen, B., Hofmann, M., Zieger, J., Krause, R., Kriesfeld, L., Smith, J.,

2019. New high-resolution age data from the Ediacaran–Cambrian boundary indicate rapid, ecologically driven onset of the Cambrian explosion. Terra Nova 31, 49–58. https://doi.org/10.1111/ter.12368
Lu, M., Zhu, M., Zhang, J., Shields-Zhou, G., Li, G., Zhao, F., Zhao, X., Zhao, M., 2013. The DOUNCE event at the top of the Ediacaran Doushantuo Formation, South China: Broad stratigraphic occurrence and non-diagenetic origin. Precambrian Res., Biogeochemical changes across the Ediacaran-Cambrian transition in South China 225, 86–109. https://doi.org/10.1016/j.precamres.2011.10.018
Macdonald, F.A., Jones, D.S., Schrag, D.P., 2009. Stratigraphic and tectonic implications of a newly discovered glacial diamictite–cap carbonate couplet in southwestern Mongolia. Geology 37, 123–126. https://doi.org/10.1130/G24797A.1
Narbonne, G.M., Saylor, B.Z., Grotzinger, J.P., 1997. The youngest Ediacaran fossils from southern Africa. J. Paleontol. 953–967.
Payne, J.L., Turchyn, A.V., Paytan, A., DePaolo, D.J., Lehrmann, D.J., Yu, M., Wei, J., 2010. Calcium isotope constraints on the end-Permian mass extinction. Proc. Natl. Acad. Sci. 107, 8543–8548. https://doi.org/10.1073/pnas.0914065107
Penny, A., Wood, R., Curtis, A., Bowyer, F., Tostevin, R., Hoffman, K.-H., 2014. Ediacaran metazoan reefs from the Nama Group, Namibia. Science 344, 1504–1506.
Penny, A.M., Wood, R.A., Zhuravlev, A.Yu., Curtis, A., Bowyer, F., Tostevin, R., 2016. Intraspecific variation in an Ediacaran skeletal metazoan: Namacalathus from the Nama Group, Namibia. Geobiology. https://doi.org/10.1111/gbi.12205
Peters, S.E., Gaines, R.R., 2012. Formation of the 'Great Unconformity' as a trigger for the Cambrian explosion. Nature 484, 363.
Pruss, S.B., Blättler, C.L., Macdonald, F.A., Higgins, J.A., 2018. Calcium isotope evidence that the earliest metazoan biomineralizers formed aragonite shells. Geology 46, 763–766. https://doi.org/10.1130/G45275.1
Rennie, V.C.F., Turchyn, A.V., 2014. The preservation of and in carbonate-associated sulfate during marine diagenesis: A 25 Myr test case using marine sediments. Earth Planet. Sci. Lett. 395, 13–23. https://doi.org/10.1016/j.epsl.2014.03.025
Ries, J.B., Fike, D.A., Pratt, L.M., Lyons, T.W., Grotzinger, J.P., 2009. Superheavy pyrite (δ34Spyr > δ34SCAS) in the terminal Proterozoic Nama Group, southern Namibia: A consequence of low seawater sulfate at the dawn of animal life. Geology 37, 743–746. https://doi.org/10.1130/G25775A.1
Rothman, D.H., Hayes, J.M., Summons, R.E., 2003. Dynamics of the Neoproterozoic carbon cycle. Proc. Natl. Acad. Sci. 100, 8124–8129. https://doi.org/10.1073/pnas.0832439100
Rudge, J.F., Reynolds, B.C., Bourdon, B., 2009. The double spike toolbox. Chem. Geol. 265, 420–431. https://doi.org/10.1016/j.chemgeo.2009.05.010
Sawaki, Y., Ohno, T., Tahata, M., Komiya, T., Hirata, T., Maruyama, S., Windley, B.F., Han, J., Shu, D., Li, Y., 2010. The Ediacaran radiogenic Sr isotope excursion in the Doushantuo Formation in the Three Gorges area, South China. Precambrian Res. 176, 46–64. https://doi.org/10.1016/j.precamres.2009.10.006
Sawaki, Y., Tahata, M., Ohno, T., Komiya, T., Hirata, T., Maruyama, S., Han, J., Shu, D., 2013. The anomalous Ca cycle in the Ediacaran ocean: Evidence from Ca isotopes preserved in

carbonates in the Three Gorges area, South China. Gondwana Res. https://doi.org/10.1016/j.gr.2013.03.008
Saylor, B.Z., 2003. Sequence Stratigraphy and Carbonate-Siliciclastic Mixing in a Terminal Proterozoic Foreland Basin, Urusis Formation, Nama Group, Namibia. J. Sediment. Res. 73, 264–279. https://doi.org/10.1306/082602730264
Saylor, B.Z., Kaufman, A.J., Grotzinger, J.P., Urban, F., 1998. A Composite Reference Section for Terminal Proterozoic Strata of Southern Namibia. SEPM J. Sediment. Res. 68. https://doi.org/10.1306/D426893C-2B26-11D7-8648000102C1865D
Schmitt, A.-D., Gangloff, S., Cobert, F., Lemarchand, D., Stille, P., Chabaux, F., 2009. High performance automated ion chromatography separation for Ca isotope measurements in geological and biological samples. J. Anal. At. Spectrom. 24, 1089–1097. https://doi.org/10.1039/B903303C
Schrag, D.P., Higgins, J.A., Macdonald, F.A., Johnston, D.T., 2013. Authigenic carbonate and the history of the global carbon cycle. Science 339, 540–543.
Scotese, C.R., 2009. Late Proterozoic plate tectonics and palaeogeography: a tale of two supercontinents, Rodinia and Pannotia. Geol. Soc. Lond. Spec. Publ. 326, 67–83. https://doi.org/10.1144/SP326.4
Shields, G.A., Mills, B.J.W., Zhu, M., Raub, T.D., Daines, S.J., Lenton, T.M., 2019. Unique Neoproterozoic carbon isotope excursions sustained by coupled evaporite dissolution and pyrite burial. Nat. Geosci. https://doi.org/10.1038/s41561-019-0434-3
Simkiss, K., 1977. Biomineralization and detoxification. Calcif. Tissue Res. 24, 199–200. https://doi.org/10.1007/BF02223316
Solomon, M., Rafter, T.A., Dunham, K.C., 1971. Sulphur and oxygen isotope studies in the northern Pennines in relation to ore diagenesis. Trans. Inst. Min. Metall. 259–275.
Steuber, T., Veizer, J., 2002. Phanerozoic record of plate tectonic control of seawater chemistry and carbonate sedimentation. Geology 30, 1123–1126. https://doi.org/10.1130/0091-7613(2002)030<1123:PROPTC>2.0.CO;2
Strauss, H., Banerjee, D.M., Kumar, V., 2001. The sulfur isotopic composition of Neoproterozoic to early Cambrian seawater—evidence from the cyclic Hanseran evaporites, NW India. Chem. Geol. 175, 17–28.
Tang, J., Dietzel, M., Böhm, F., Köhler, S.J., Eisenhauer, A., 2008. Sr2+/Ca2+ and 44Ca/40Ca fractionation during inorganic calcite formation: II. Ca isotopes. Geochim. Cosmochim. Acta 72, 3733–3745. https://doi.org/10.1016/j.gca.2008.05.033
Tipper, E.T., Gaillardet, J., Galy, A., Louvat, P., Bickle, M.J., Capmas, F., 2010. Calcium isotope ratios in the world's largest rivers: A constraint on the maximum imbalance of oceanic calcium fluxes. Glob. Biogeochem. Cycles 24. https://doi.org/10.1029/2009GB003574
Tostevin, R., Clarkson, M.O., Gangl, S., Shields, G.A., Wood, R.A., Bowyer, F., Penny, A.M., Stirling, C.H., 2019. Uranium isotope evidence for an expansion of anoxia in terminal Ediacaran oceans. Earth Planet. Sci. Lett. 506, 104–112. https://doi.org/10.1016/j.epsl.2018.10.045
Tostevin, R., He, T., Turchyn, A.V., Wood, R.A., Penny, A.M., Bowyer, F., Antler, G., Shields, G.A., 2017. Constraints on the late Ediacaran sulfur cycle from carbonate associated sulfate. Precambrian Res. 290, 113–125. https://doi.org/10.1016/j.precamres.2017.01.004

975 Tostevin, R., Shields, G.A., Tarbuck, G.M., He, T., Clarkson, M.O., Wood, R.A., 2016a. Effective
976 use of cerium anomalies as a redox proxy in carbonate-dominated marine settings.
977 Chem. Geol. 438, 146–162. https://doi.org/10.1016/j.chemgeo.2016.06.027
978 Tostevin, R., Wood, R.A., Shields, G.A., Poulton, S.W., Guilbaud, R., Bowyer, F., Penny, A.M., He,
979 T., Curtis, A., Hoffmann, K.H., Clarkson, M.O., 2016b. Low-oxygen waters limited
980 habitable space for early animals. Nat. Commun. 7.
981 https://doi.org/10.1038/ncomms12818
982 Turchyn, A.V., DePaolo, D.J., 2011. Calcium isotope evidence for suppression of carbonate
983 dissolution in carbonate-bearing organic-rich sediments. Geochim. Cosmochim. Acta 75,
984 7081–7098. https://doi.org/10.1016/j.gca.2011.09.014
985 Vermeij, G.J., 1989. The Origin of Skeletons. PALAIOS 4, 585–589.
986 https://doi.org/10.2307/3514748
987 Wood, R., Bowyer, F., Penny, A., Poulton, S.W., 2018. Did anoxia terminate Ediacaran benthic
988 communities? Evidence from early diagenesis. Precambrian Res. 313, 134–147.
989 https://doi.org/10.1016/j.precamres.2018.05.011
990 Wood, R.A., 2011. Paleoecology of the earliest skeletal metazoan communities: Implications for
991 early biomineralization. Earth-Sci. Rev. 106, 184–190.
992 https://doi.org/10.1016/j.earscirev.2011.01.011
993 Wood, R.A., Curtis, A., 2015. Extensive metazoan reefs from the Ediacaran Nama Group,
994 Namibia: the rise of benthic suspension feeding. Geobiology 13, 112–122.
995 https://doi.org/10.1111/gbi.12122
996 Wood, R.A., Grotzinger, J.P., Dickson, J.A.D., 2002. Proterozoic Modular Biomineralized
997 Metazoan from the Nama Group, Namibia. Science 296, 2383–2386.
998 https://doi.org/10.1126/science.1071599
999 Wood, R.A., Ivantsov, A.Y., Zhuravlev, A.Y., 2017a. First macrobiota biomineralization was
1000 environmentally triggered. Proc R Soc B 284, 20170059.
1001 https://doi.org/10.1098/rspb.2017.0059
1002 Wood, R.A., Poulton, S.W., Prave, A.R., Hoffmann, K.-H., Clarkson, M.O., Guilbaud, R., Lyne,
1003 J.W., Tostevin, R., Bowyer, F., Penny, A.M., Curtis, A., Kasemann, S.A., 2015. Dynamic
1004 redox conditions control late Ediacaran ecosystems in the Nama Group, Namibia.
1005 Precambrian Res. 261, 252–271.
1006 Wood, R.A., Zhuravlev, A.Y., Sukhov, S.S., Zhu, M., Zhao, F., 2017b. Demise of Ediacaran
1007 dolomitic seas marks widespread biomineralization on the Siberian Platform. Geology
1008 45, 27–30. https://doi.org/10.1130/G38367.1
1009 Wu, N., Farquhar, J., Fike, D.A., 2015. Ediacaran sulfur cycle: Insights from sulfur isotope
1010 measurements (Δ33S and δ34S) on paired sulfate-pyrite in the Huqf Supergroup of
1011 Oman. Geochim. Cosmochim. Acta 164, 352–364.
1012 Zhang, F., Xiao, S., Kendall, B., Romaniello, S.J., Cui, H., Meyer, M., Gilleaudeau, G.J., Kaufman,
1013 A.J., Anbar, A.D., 2018. Extensive marine anoxia during the terminal Ediacaran Period.
1014 Sci. Adv. 4, eaan8983. https://doi.org/10.1126/sciadv.aan8983
1015 Zhuravlev, A.Yu., Wood, R.A., 2008. Eve of biomineralization: Controls on skeletal mineralogy.
1016 Geology 36, 923–926. https://doi.org/10.1130/G25094A.1
1017